

# Numerical simulation of electrospaying in the cone-jet mode

M. Gamero-Castaño<sup>1,†</sup> and M. Magnani<sup>1</sup>

<sup>1</sup>Department of Mechanical and Aerospace Engineering, University of California, Irvine, CA 92697, USA

(Received 30 May 2018; revised 27 September 2018; accepted 10 October 2018; first published online 16 November 2018)

This article solves numerically the equations of the leaky-dielectric model applied to cone jets. The solution is a function of the properties of the fluid and its flow rate, universal in that it does not depend on the geometry and potential of the electrodes. This is made possible by the use of the potential field generated by a semi-infinite Taylor cone as a far-field boundary condition. The numerical solution yields the current emitted by the electrospay, which compares well with experimental data, and detailed information about the velocity, surface charge, electric field and the position of the free surface. These characteristics are generally inaccessible through experiments, and are needed to understand the relative importance of competing processes and the dominant physics. The simulations investigate the liquids tributyl phosphate and propylene carbonate (dielectric constants of 8.91 and 64.9 respectively), in a wide range of electrical conductivities and flow rates. The simulations show that the position of the surface, expressed in units of the characteristic length  $r_c$ , is largely invariant regardless of the physical properties and flow rates of the liquids. The surface charge falls below its equilibrium value along the transition from cone to jet, with a deficit that increases with the ratio between the electrical relaxation and flow residence times. Several characteristics of the cone jet are functions of the dielectric constant, which is consistent with the importance of charge relaxation effects (i.e. with the absence of surface charge equilibrium). The electric energy transferred to the transition region is largely transformed into viscous and ohmic dissipation, and conversion into kinetic energy only dominates once most of the current is fixed on the surface.

**Key words:** aerosols/atomization, electrohydrodynamic effects, interfacial flows (free surface)

---

## 1. Introduction

Electrospaying is an atomization technique characterized by the strong interaction between surface tension, electrical and hydrodynamic stresses. Typically a liquid is fed to the tip of a tubular emitter, and an electric potential applied with respect to a facing surface in an axisymmetric configuration. The shape adopted by the fluid exiting the emitter electrode depends on the strength of the electrification and the

<sup>†</sup>Email address for correspondence: [mgameroc@uci.edu](mailto:mgameroc@uci.edu)

properties and flow rate of the fluid. Multiple electro spraying modes have been studied (Cloupeau & Prunet-Foch 1990), and several have been found useful in technological applications such as electro spray mass spectrometry (Fenn *et al.* 1989), microparticle encapsulation (Loscertales *et al.* 2002), nanodroplet sputtering (Borrajó-Pelaez, Saiz & Gamero Castano 2015), space propulsion (Grustan-Gutierrez & Gamero-Castaño 2017), electro spinning (Sun *et al.* 2006), etc. This article focuses on the cone-jet mode (Cloupeau & Prunet-Foch 1989; Fernández de la Mora 2007), characterized by the formation of a steady conical region anchored at the base of the emitter, and from which a slender steady jet is formed with a diameter orders of magnitude smaller than that of the base of the cone. The jet is accelerated by the electric field acting on charge migrated to its surface, and its diameter is determined by the physical properties and flow rate of the liquid. In most applications the jet is allowed to break by capillary instability, to produce a spray or beam of similar droplets with radii as small as a few nanometres. Although the formation of these jets and associated sprays do not in principle require a much larger conical meniscus, the cone-jet configuration, with its disparity of length scales, is of interest for two reasons: first, it decouples the diameter of the jet and associated droplets from that of the emitter, making it possible to generate jets orders of magnitude smaller than the size of orifices that can be practically made; and second, the much larger cone provides a distinct background electric field for the jet, making its electrohydrodynamics largely insensitive to the geometry and potential of the electrodes. Thus, the analysis of the cone-jet geometry yields a solution for the electro spray current, the position of the free surface, the jet diameter, etc. that is only a function of the physical properties of the fluid and its flow rate.

Two distinct approaches have been used to analyse cone jets: zeroth-order models use simplifying hypothesis and the identification of key balances to derive scaling laws for the characteristics of cone jets; and continuum models in the form of differential equations that need to be solved numerically. Fernández de la Mora & Loscertales (1994) argue that the formation of the jet is caused by the departure of the surface charge from the equilibrium, a condition that takes place when the flow residence time becomes comparable to the electrical relaxation time. At this point Taylor's (1964) electrostatic solution, consisting of a cone with a  $49.29^\circ$  half-angle, breaks down, and a different geometry such as a jet must develop. From this balance Fernández de la Mora and Loscertales find that the diameter of the jet scales with the characteristic length  $r_{FM} = (\varepsilon\varepsilon_0Q/K)^{1/3}$ ;  $\varepsilon_0$  stands for the permittivity of the vacuum, and  $\varepsilon$ ,  $K$  and  $Q$  for the dielectric constant (or relative permittivity), the electrical conductivity and the flow rate of the liquid. Furthermore, taking into account that in this region the net current is comparable to the surface current, and that the surface charge is comparable to the one associated with Taylor's solution, they find the electro spray current to scale with  $(\gamma KQ)^{1/2}$ , where  $\gamma$  is the surface tension of the liquid. Both scaling laws compare well with the average droplet diameter and current measured for a variety of liquids. Alternatively, Gañán-Calvo (1997) proposes that the surface charge is near equilibrium everywhere in the cone jet, and finds that the diameter of the jet scales with  $r_c = (\rho\varepsilon_0Q^3/(\gamma K))^{1/6}$ , where  $\rho$  is the density of the liquid. This length scale is derived from a balance between kinetic energy and electric energy in the transition region, and compares with droplet diameter data better than the  $r_{FM}$  scaling (Gamero-Castaño & Hruby 2002). Under these assumptions, the dielectric constant does not play any role in the characteristics of cone jets. Numerical solutions of continuum models have been developed by Higuera (2003) and Herrada *et al.* (2012) among others. Both solve the equations

of the leaky-dielectric model applied to cone jets (Saville 1997). Higuera simulates a relatively small area surrounding the transition region between cone and jet, using far-field boundary conditions derived from Taylor’s electrostatic solution (Taylor 1964). Higuera simulates two values of the dielectric constant, 5 and 50, at flow rates that are generally smaller than those realized experimentally. Although the simulations are not directly validated with experiments, the reported currents compare well with extrapolated experimental data for liquids with similar dielectric constants. Higuera discusses that the surface charge is not in equilibrium for a dielectric constant of 50 at the lowest flow rates, but this could be an artefact of the low flow rates and may not hold under actual electrospraying conditions. Herrada *et al.* include the emitter in the simulation domain. There is not a large disparity between the diameters of the jet and the emitter and therefore the numerical solution is a function of the geometry and potentials of the electrodes. The position of the free surface compares well with experimental measurements, while current values differ by 17%.

This article solves the equations of the leaky-dielectric model in an extended area surrounding the transition region, using Taylor’s potential as a far-field boundary condition, and with the goal of resolving the physics of electrospraying under operational conditions typical of experimental work. In particular, we are most interested in examining the role played by the dielectric constant and whether the surface charge is equilibrated on the free surface; obtaining improved expressions for the characteristics cone jets beyond existing scaling laws; and investigating how the electric power transferred to the cone jet is converted into kinetic energy and dissipation.

## 2. Model and numerical scheme

Figure 1 shows the main features of the axisymmetric computational domain. Liquid flows through a conical region prolonged by a jet and surrounded by a vacuum. The cone jet is enclosed by curves  $\Gamma_1$ ,  $\Gamma_2^i$  and  $\Gamma_3^i$ , and the surrounding vacuum by  $\Gamma_1$  and the circular arc  $\Gamma_2^o$ . The associated surfaces of revolution are termed  $\Sigma_1$ ,  $\Sigma_2^i$ , etc.  $\Gamma_1$  is the generatrix of the free surface,  $\{x_o, R_o\}$  and  $\{x_f, R_f\}$  are its upstream and downstream end points and  $\mathbf{n}$  and  $\mathbf{t}$  are its normal and tangential unit vectors. The unknowns of the model are the velocity  $\mathbf{v}$ , pressure  $p$  and the electric potential  $\phi^i$  fields inside the fluid domain; the electric potential in the vacuum,  $\phi^o$ ; and the surface charge  $\sigma$  and the position of the free surface,  $r = R(x)$ . All fields are steady and axisymmetric. The equations of conservation of mass and charge, the Navier–Stokes equations, and Laplace’s equation for the electrical potential describe the electro-hydrodynamics and geometry of the cone jet (Melcher & Taylor 1969; Saville 1997; Higuera 2003). The following scales for length  $r_c$ , electric current  $I_c$ , velocity  $v_c$ , pressure  $p_c$ , electric field  $E_c$ , electric potential  $\phi_c$  and surface charge  $\sigma_c$  are used to non-dimensionalize the equations:

$$r_c = \left( \frac{\rho \epsilon_0 Q^3}{\gamma K} \right)^{1/6}, \quad I_c = (\gamma K Q)^{1/2}, \quad v_c = \frac{Q}{\pi r_c^2} \tag{2.1a-c}$$

$$p_c = \frac{\gamma}{r_c}, \quad E_c = \frac{I_c}{\pi r_c^2 K}, \quad \phi_c = r_c E_c, \quad \sigma_c = \frac{I_c}{2\pi r_c v_c}. \tag{2.2a-d}$$

The  $r_c$  scale was first proposed by Gañán-Calvo, Dávila & Barrero (1997) for the radius of the jet, and our model employs it for both the radial and axial directions (Gamero-Castaño 2010). The current emitted by cone jets is known to scale with  $I_c$  (Fernández de la Mora & Loscertales 1994). All other scales follow from these two

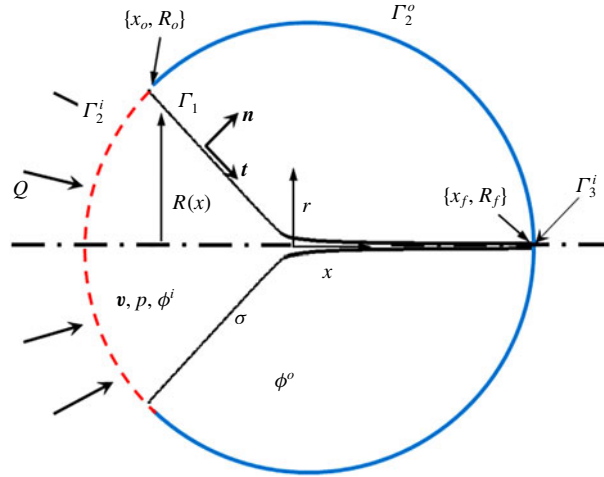


FIGURE 1. (Colour online) Computational domain.

choices and the goal of making the non-dimensional variables of order one in the cone-to-jet transition region. The resulting non-dimensional equations of conservation of mass and momentum, and Laplace’s equation inside the fluid are:

$$\nabla \cdot \mathbf{v} = 0, \quad \mathbf{v} \cdot \nabla \mathbf{v} = -\frac{\pi^2}{\Pi_Q^{1/2}} \nabla p + \frac{\pi}{\Pi_Q^{1/2} Re} \nabla^2 \mathbf{v}, \quad \nabla^2 \phi^i = 0. \quad (2.3a-c)$$

Note that the symbols used earlier for the dimensional variables denote now their dimensionless counterparts, while dimensional variables will be henceforth topped by a tilde. Laplace’s equation for the potential in the surrounding vacuum is:

$$\nabla^2 \phi^o = 0 \quad (2.4)$$

and the equations of conservation of charge, balance of stresses (projected on the  $\mathbf{n}$  and  $\mathbf{t}$  vectors), the kinematic condition at the surface and the jump of the components of electric field at the fluid–vacuum interface are:

$$\frac{d}{dx}(Rv_S\sigma) = 2RE_n^i(1 + R^2)^{1/2}, \quad (2.5)$$

$$\frac{R^2 - RR'' + 1}{R(1 + R^2)^{3/2}} = p + \frac{2}{\pi Re} \frac{R'R''u}{1 + R^2} + \frac{1}{2\pi^2 \Pi_Q^{1/2}} (E_n^{o2} - \varepsilon E_n^{i2}) + \frac{1}{2\pi^2 \Pi_Q^{1/2}} (\varepsilon - 1) E_t^2, \quad (2.6)$$

$$\mathbf{t} \cdot \boldsymbol{\tau} \cdot \mathbf{n} = \frac{2R' \left( \frac{\partial v}{\partial r} - \frac{\partial u}{\partial x} \right) + (1 - R^2) \left( \frac{\partial u}{\partial r} + \frac{\partial v}{\partial x} \right)}{1 + R^2} = \frac{Re}{2} \sigma E_t, \quad (2.7)$$

$$\mathbf{v} \cdot \mathbf{n} = 0, \quad \sigma = \frac{2}{\pi \Pi_Q^{1/2}} (E_n^o - \varepsilon E_n^i), \quad E_t^o = E_t^i = E_t; \quad (2.8a-c)$$

$v_S$  stands for the fluid speed at the free surface,  $u$  and  $v$  are the axial and radial components of the velocity and  $\boldsymbol{\tau}$  is the viscous stress tensor. The dimensionless equations include three independent dimensionless numbers, namely the dimensionless

flow rate  $\Pi_Q = \rho K Q / (\gamma \epsilon_o)$ , the group  $Re = (\rho \epsilon_o \gamma^2 / (\mu^3 K))^{1/3}$  referred to in the literature as the electrohydrodynamic Reynolds number and the dielectric constant  $\epsilon$ .

The Taylor potential

$$\phi_T(x, r) = -4.2283 \Pi_Q^{1/4} (x^2 + r^2)^{1/4} P_{1/2} \left( \frac{x}{\sqrt{x^2 + r^2}} \right) \tag{2.9}$$

is used as boundary condition at  $\Gamma_2^o$ , while the upstream and downstream boundaries of the cone jet,  $\Gamma_2^i$  and  $\Gamma_3^i$ , are modelled as equipotential surfaces.  $P_{1/2}$  is the Legendre function of the first kind of degree 1/2. The  $\Pi_Q^{1/4}$  factor results from making the Taylor potential dimensionless with the scales  $r_c$  and  $\phi_c$ . The Taylor potential is the field outside an equipotential semi-infinite, hydrostatic cone in which the capillary tension and the electrostatic stress fully balance each other (Taylor 1964). The solution requires a half-angle  $\alpha_T$  of 49.29° for the cone, in good agreement with observations. In experimental cone jets with jet diameters orders of magnitude smaller than the dimensions of the electrodes, the Taylor potential is a good approximation for an extended region far from both the base of the cone and the area where it transitions into a jet. Furthermore its use as the far-field boundary condition eliminates dependencies on the geometry and the potentials of the electrodes. This agrees with the weak dependence of the electrospray current on the emitter potential and geometry observed in experiments, as long as the diameter of the jet is orders of magnitude smaller than that of the emitter.

A spherical velocity profile with net flow rate  $Q$  is imposed at the upstream boundary:

$$\mathbf{v}(\Gamma_2^i) = -\frac{1}{2(1 - \cos \alpha_T)(x^2 + r^2)^{3/2}} \mathbf{r}. \tag{2.10}$$

Finally, the initial point  $\{x_o, R_o\}$  is modelled as a continuation of the static Taylor cone that implicitly exists upstream of the computational domain. This fixes the radius, the slope, the pressure (the electrostatic stress is fully balanced by capillary tension) and the surface charge at this point:

$$R(x_o) = x_o \tan \alpha_T, \quad R'(x_o) = \tan \alpha_T, \quad p(R(x_o)) = 0, \quad \sigma(x_o) = \frac{2}{\pi \Pi_Q^{1/2}} \left. \frac{d\phi_T}{dn} \right|_{R(x_o)}. \tag{2.11a-d}$$

The Navier–Stokes and mass conservation equations are solved in the streamfunction/vorticity formulation. In axisymmetric problems this reduces the system of three coupled equations for the two velocity components and the pressure, to a system of two coupled equations for two unknowns: the streamfunction  $\psi$ , and the vorticity  $\omega$ ,  $\omega = \partial v / \partial x - \partial u / \partial r$ . Once these two fields are calculated, the two velocity components can be obtained from the streamfunction,  $u = (1/r)(\partial \psi / \partial r)$ ,  $v = -(1/r)(\partial \psi / \partial x)$  and the pressure by integrating the momentum equation. The non-dimensional streamfunction and vorticity equations are:

$$\frac{\partial^2 \psi}{\partial x^2} + \frac{\partial^2 \psi}{\partial r^2} - \frac{1}{r} \frac{\partial \psi}{\partial r} = -r\omega, \tag{2.12}$$

$$\frac{\partial^2 \omega}{\partial x^2} + \frac{\partial}{\partial r} \left( \frac{1}{r} \frac{\partial (r\omega)}{\partial r} \right) = \frac{\Pi_Q^{1/2} Re}{\pi} \left( u \frac{\partial \omega}{\partial x} + v \frac{\partial \omega}{\partial r} - \frac{v}{r} \omega \right), \tag{2.13}$$

with boundary conditions:

$$\psi(x, 0) = 0, \quad \psi(R(x)) = \frac{1}{2}, \quad \psi(\Gamma_2^i) = \int_{x_o}^x S_U(x)(uS'_U - v) dx, \quad \psi(\Gamma_3^i) = \frac{1}{2} \left( \frac{r}{R(x_f)} \right)^2 \tag{2.14a-d}$$

$$\omega(x, 0) = 0, \quad \omega(\Gamma_1) = \frac{2R''}{R^2(1 + R^2)} \frac{d\psi}{dn} - \frac{Re}{2} \sigma E_t, \quad \omega(\Gamma_2^i) = 0, \quad \left. \frac{\partial \omega}{\partial x} \right|_{\Gamma_3^i} = 0. \tag{2.15a-d}$$

The boundary conditions are associated with the imposed upstream velocity profile ( $r = S_U(x)$  defines the curve  $\Gamma_2^i$ ), the kinematic condition at the surface, the axial symmetry of the problem and soft exit conditions. Equation (2.15b) is derived from (2.7).

Finally, the Navier–Stokes equation is integrated along  $\Gamma_1$  to obtain the pressure at the surface:

$$p_s(x) = p_s(x_o) - \frac{\Pi_Q^{1/2}}{2\pi^2} (v_s^2(x) - v_s^2(x_o)) - \frac{1}{\pi Re} \int_{x_o}^x \left( \frac{\omega}{R} + \frac{1 + R^2}{R} \frac{d\omega}{dn} \right) dx. \tag{2.16}$$

Figure 2 summarizes the algorithm used to solve the system of equations. We combine the equations into three groups referred to as the fluid problem, (2.12), (2.13) and boundary conditions (2.14)–(2.15); the electric problem, (2.3c), (2.4), (2.5) and boundary conditions (2.8b), (2.9), (2.12) and equipotential  $\Gamma_2^i$  and  $\Gamma_3^i$  surfaces; and the Young–Laplace equation (2.6) with initial conditions (2.11a) and (2.11b). The fluid and electric problems can be solved for a given surface profile  $R_k(x)$ . The equations are nonlinear and coupled through the  $\sigma E_t$  and  $v_s$  terms in (2.15b) and (2.5), and an iterative scheme is used: we assume a starting surface velocity and solve the electric problem for the given  $R_k(x)$ ; the resulting  $\sigma E_t$  stress is used to solve the fluid problem; the surface velocity is then updated. These steps are repeated until the integrals of the square of the residue of (2.12) and (2.13) become smaller than a desired value. Upon convergence of this inner loop, the calculated velocity, pressure and electric fields, and the assumed surface profile  $R_k(x)$  will not in general fulfil the Young–Laplace equation, and the least-squares weighted residual method is used to generate an improved surface profile  $R_{k+1}(x)$ . That is, we minimize the integral:

$$\int_{\Gamma_1} \left[ \frac{R^2 - RR'' + 1}{R(1 + R^2)^{3/2}} - RHS_k(x) \right]^2 dx, \tag{2.17}$$

$$RHS_k(x) = p + \frac{2}{\pi Re} \frac{R'R''u}{1 + R^2} + \frac{1}{2\pi^2 \Pi_Q^{1/2}} (E_n^{o2} - \varepsilon E_n^{i2}) + \frac{1}{2\pi^2 \Pi_Q^{1/2}} (\varepsilon - 1) E_t^2, \tag{2.18}$$

where (2.18) is evaluated with the solution from iteration  $k$ . The weighted residue scheme is implemented with a surface profile discretized into  $n$  nodes,  $R_j$ , and the integral written as a function of the vector  $\mathbf{X} = \{R_2, R_3, \dots, R_n\}$  for given values of  $RHS_k(x)$  and the initial conditions  $R_1, R'_1$ . Differentiating with respect to  $R_2, \dots, R_n$  yields a system of  $n - 1$  nonlinear equations  $S_j(\mathbf{X})$ , and the improved profile  $R_{k+1}$  is calculated by taking a small step  $\delta$  in the direction of the first iteration in a Newton–Raphson scheme:

$$\mathbf{X}_{k+1} = \mathbf{X}_k - [\mathbf{J}^{-1} \cdot \mathbf{S}(\mathbf{X})] \delta, \quad \mathbf{J} = \nabla \mathbf{S}(\mathbf{X}_k). \tag{2.19a,b}$$

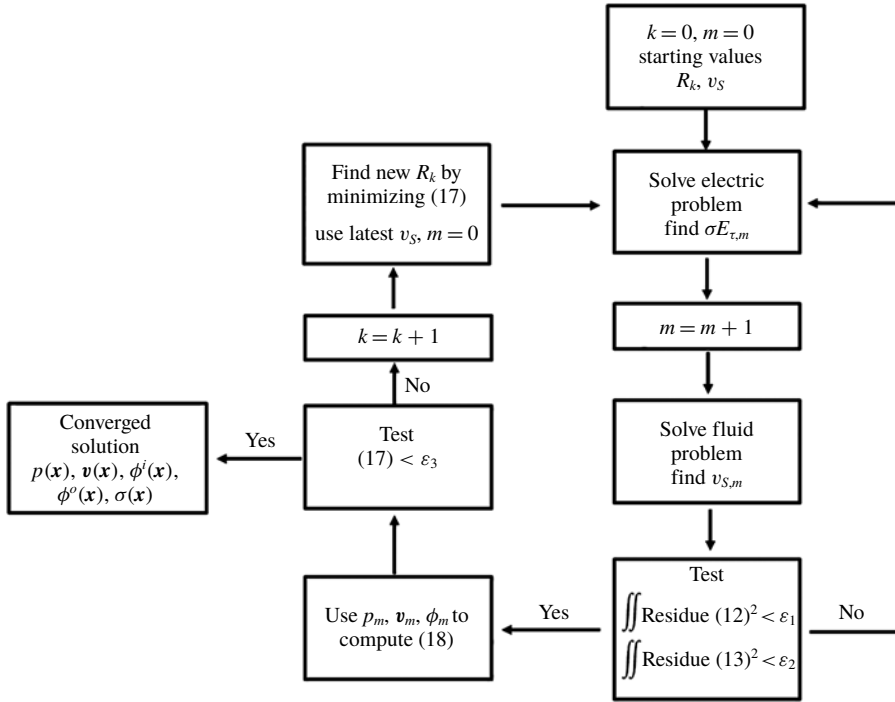


FIGURE 2. Algorithm used for solving the system of equations.

The fluid and electric problems are computed again with the updated surface profile  $R_{k+1}$ , and the steps are repeated until (2.17) is smaller than a desired value.

Equations (2.3c) and (2.4) for the electric potentials are solved using the boundary element method (BEM) with linear elements (Bakr 1986). The resulting system of linear algebraic equations is supplemented with those from the discretization of (2.5) using centred finite differences. The electric problem is then solved at once by direct matrix inversion. The partial differential equations (PDEs) of the fluid problem, (2.12) and (2.13), are discretized using centred finite differences in an orthogonal grid (Fletcher 1988). The grid is built on a generalized curvilinear coordinate  $\{\xi, \eta\}$  system such that the free surface and the axis are lines of constant  $\eta$ , while  $\Gamma_2^i$  and  $\Gamma_3^i$  are lines of constant  $\xi$ . The algebraic equations are linearized, and solved iteratively by direct matrix inversion. Figure 3(a) shows a section of the orthogonal grid. Because the fluid domain transitions from a two-dimensional cone to a slender jet, we employ three successive grids with decreasing numbers of nodes in the  $\eta$  direction: the grid placed in the cone typically has 20 nodes in the  $\eta$  direction, the central grid has 10 nodes and the grid placed in the jet has 4 nodes. The central grid is centred at the maximum of  $R''(x)$  and has uniform spacing in the axial direction, while the spacing in the cone and jet grids is non-uniform. The streamfunction, vorticity and their derivatives in the  $\xi$  direction are required to be continuous at the interface between adjacent grids. Figure 3(b) shows a typical discretization of the boundaries for the boundary element method. 426, 128, 34 and 4 nodes are inserted in  $\Gamma_1$ ,  $\Gamma_2^o$ ,  $\Gamma_2^i$  and  $\Gamma_3^i$  respectively. The nodes are distributed uniformly in  $\Gamma_2^o$ ,  $\Gamma_2^i$  and  $\Gamma_3^i$ , and have a variable density in  $\Gamma_1$ : along the surface of the central grid, where the changes in the electric field and surface charge are most intense, we place one BEM node at the

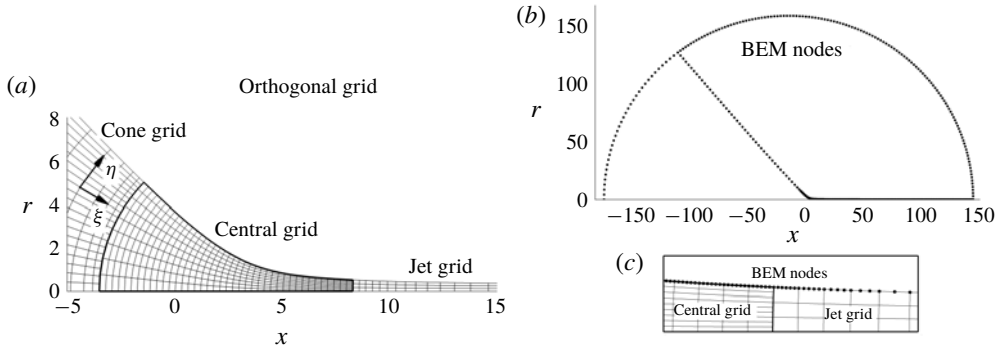


FIGURE 3. (a) Detail of the orthogonal grid employed in the solution of the streamfunction and vorticity PDEs; (b) BEM discretization; (c) detail of the BEM nodes and the orthogonal grid in the interface between central and jet grids.

position of each grid node, plus five equally spaced nodes in between (i.e. there are six BEM elements between consecutive central grid nodes); upstream and downstream of the central grid we place one BEM node at the position of each grid node, and insert additional nodes near the ends of the central grid so that the length of the BEM elements changes smoothly (see figure 3c).

### 3. Results and discussion

The electro spraying conditions investigated include two dielectric constants, 8.91 and 64.9; two values of the Reynolds number for each dielectric constant ( $Re = 0.29$  and  $1.12$  for  $\varepsilon = 8.91$ , and  $Re = 0.40$  and  $0.74$  for  $\varepsilon = 64.9$ ); and a range of flow rates for each Reynolds number. Gamero-Castaño (2010) has characterized these electro spraying conditions with solutions of the liquids tributyl phosphate ( $\varepsilon = 8.91$ ) and propylene carbonate ( $\varepsilon = 64.9$ ), and these measurements will be used to validate the numerical results. The flow rates simulated coincide with the ranges measured except for tributyl phosphate at  $Re = 1.12$ , for which the simulations extend the measurements to much lower and higher flow rates (the ratio between the highest and lowest flow rate is 350). In particular, the lowest flow rate for this solution is clearly outside the stable range observed in our experiments, and the numerical solution may correspond to a linearly unstable base state (Gañán-Calvo *et al.* 2018). A circular arc  $\Gamma_2^o$  with a radius of 144.0 is employed in the simulations of tributyl phosphate, while the radius is 200.5 for propylene carbonate.

Figures 4(a) and 4(b) show the electric current emitted by the electro spray as a function of the dimensionless flow rate, both in dimensionless form and in nano-amperes. Squares and circles represent experimental and numerical data respectively. The lowest dimensionless flow rates in the experimental series are near the minimum values at which the cone jets were stable. The current in nano-amperes follows the linear law  $\tilde{I}(nA) \cong a\Pi_Q^{1/2} + b$ , which in dimensionless form translates to  $I \cong (1/I_o)(a + b\Pi_Q^{-1/2})$ ,  $I_o = (\varepsilon_0\gamma^2/\rho)^{1/2}$ . The simulations yield a negative interception  $b$  with the ordinate,  $-1.96$  nA for tributyl phosphate and  $-19.7$  nA for propylene carbonate. Thus the dimensionless current asymptotes to a constant value at large  $\Pi_Q$ , and declines at the lowest  $\Pi_Q$  values. The current has a negligible dependence on the Reynolds number, while is a stronger function of the dielectric constant: the



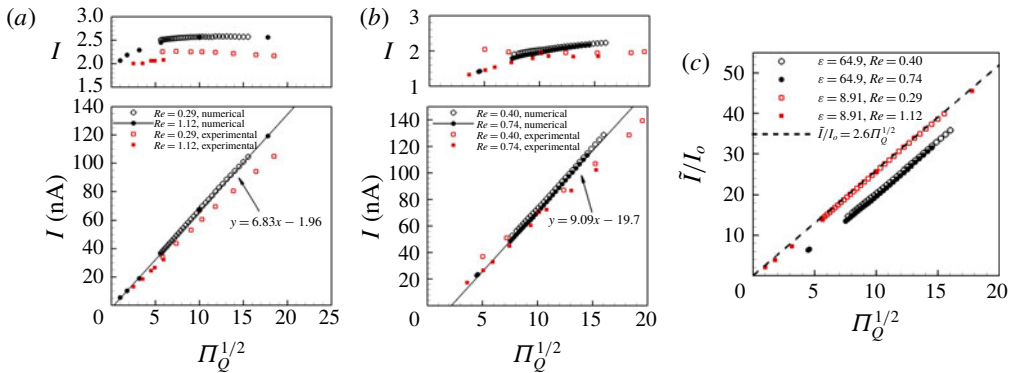


FIGURE 4. (Colour online) Dimensionless current  $I$  and current in nano-amperes as a function of the dimensionless flow rate parameter  $\Pi_Q$ , for (a) tributyl phosphate,  $\epsilon = 8.91$ ; and (b) propylene carbonate,  $\epsilon = 64.9$ . (c) Numerical values plotted in the form suggested by Gañán-Calvo *et al.* (2018),  $\tilde{I}/I_o = 2.6\Pi_Q^{1/2}$ .

asymptotic value of  $I$  at large flow rates is 2.5 for tributyl phosphate and 2.1 for propylene carbonate, a difference that is only due to the different dielectric constants. The numerical results compare well with the measurements: they coincide at flow rates near the minimum, and the numerical values become slightly larger at increasing flow rate. This trend occurs in all cases, and is likely due to the decreasing electrification of the experimental cone jets at increasing flow rate, compared to the conditions in the simulations: in the experiments the emitter potential was kept constant at all flow rates, while in the model the Taylor potential varies as  $\Pi_Q^{1/4}$ . The reduced electrification in the experiments manifests as a progressive enlargement of the liquid meniscus, which evolves into an expanding acorn-like shape ending in a Taylor cone at increasing flow rate. Although in experimental cone jets the current is a weak function of the emitter potential (we are unaware of any work quantifying this), it does increase with it, which qualitatively coincides with the trend in figure 4(a,b). Finally, figure 4(c) plots the numerical results together, following Gañán-Calvo's universal scaling law  $\tilde{I}/I_o = \alpha\Pi_Q^{1/2}$ . Note that the linear law used in figure 4(a,b) is similar to Gañán-Calvo's, except for the inclusion of an intercept with the y-axis and a slope that are functions of the dielectric constant. Gañán-Calvo *et al.* (2018) show that a massive number of experimental data for a large number of liquids, covering a remarkable  $\Pi_Q$  range of over five orders of magnitude, distribute closely to the universal scaling law when the constant  $\alpha$  has a value of 2.6. Although the ability of Gañán-Calvo's law to approximate the data across such a broad range of dimensionless flow rates is remarkable, it is also apparent in figure 7 of Gañán-Calvo *et al.* (2018), as well as in figure 4(c) of this article, that the data for a number of liquids separate to some extent from the universal law. For example, our results for tributyl phosphate at the largest flow rates coincide with Gañán-Calvo's law (compare the asymptotic value of 2.5 for  $I$ , with the slope of 2.6 found by Gañán-Calvo *et al.*), while the data for propylene carbonate fall below. Our numerical results suggest that the  $\tilde{I}/I_o = 2.6\Pi_Q^{1/2}$  law neglects dependencies on the dielectric constant, and that its accuracy should increase for decreasing  $\epsilon$  and increasing  $\Pi_Q$ , i.e. as the surface charge is closer to equilibrium (to be discussed later in the article). This is to be expected because Gañán-Calvo's law is derived under the assumption of surface charge equilibrium.

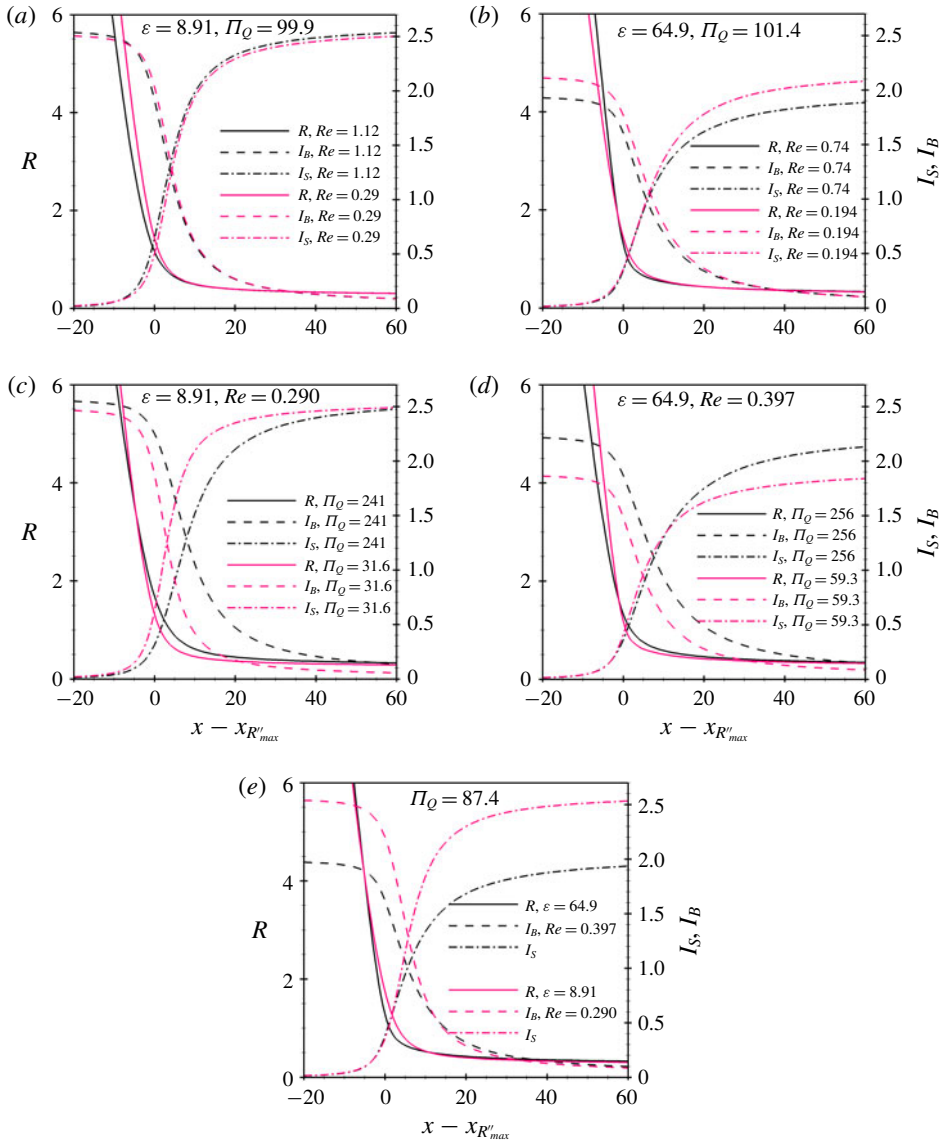


FIGURE 5. (Colour online) Position of the surface and evolution of the surface and bulk currents in the cone-to-jet transition for: (a) tributyl phosphate at fixed  $\Pi_Q$  and two  $Re$ ; (b) propylene carbonate at fixed  $\Pi_Q$  and two  $Re$ ; (c) tributyl phosphate at fixed  $Re$  and two  $\Pi_Q$ ; (d) propylene carbonate at fixed  $Re$  and two  $\Pi_Q$ ; and (e) tributyl phosphate and propylene carbonate at fixed  $\Pi_Q$ .

Figure 5(a–e) shows the position of the surface, and the evolution of the bulk and surface currents in the axial direction, for a variety of electrospaying conditions. The origin of the abscissa is set at the maximum of  $R''(x)$ ,  $x_{R''_{max}}$ . The surface and bulk currents, associated with convection of surface charge and electric conduction in the

bulk, are given by:

$$\tilde{I}_S(x) = 2\pi\tilde{R}(x)\tilde{v}_S(x)\tilde{\sigma}(x), \quad \tilde{I}_B(x) = \int_0^{R(x)} 2\pi\tilde{r}K\tilde{E}^i \cdot \nabla\Gamma \frac{d\tilde{r}}{\partial\Gamma/\partial\tilde{x}}. \quad (3.1a,b)$$

$\Gamma$  is any curve inside the cone jet that starts at the axis and ends at  $R(x)$ , e.g. in the calculations we use gridlines of constant  $\xi$ . The total current,  $= I_S(x) + I_B(x)$ , is constant due to conservation of charge. Figure 5(a,b) shows the effect of varying  $Re$  at constant  $\Pi_Q$  and  $\varepsilon$ ;  $\Pi_Q$  is varied at constant  $\varepsilon$  and  $Re$  in figure 5(c,d); and figure 5(e) illustrates the dependency on  $\varepsilon$  ( $\Pi_Q$  is fixed while the Reynolds number has a small effect). Charge is injected on the surface as the cone transitions into the jet, and the surface current progressively increases at the expense of the bulk current. The cross-over point between the surface and bulk currents is located downstream of  $x_{R''_{max}}$ . The total current is a weak function of both  $Re$  and  $\Pi_Q$  for tributyl phosphate, depends slightly on these parameters in propylene carbonate and displays a larger variation with the dielectric constant. The profiles of the cone jets are surprisingly similar despite the wide ranges of  $\Pi_Q$ ,  $Re$  and  $\varepsilon$ . The overlap is unexpected because of the presence of these parameters in the model equations, and supports the choice of  $r_c$  as the characteristic length scale in both the radial and axial directions. Note also that the transition from cone to jet is smoother, i.e. the surface profile has larger radii of curvature in an interval around  $x_{R''_{max}}$ , at both increasing dimensionless flow rate and decreasing dielectric constant. The overlap of the surface profiles when they are scaled with  $r_c$  was first discovered by Gamero-Castaño (2010) on the bases of experimental measurements of the energy deficit of electrosprayed droplets; Gamero confirmed the overlap with numerical solutions of profiles computed by Higuera (2003). Gañán-Calvo *et al.* (2018) have also confirmed the overlap using numerical simulations.

Figure 6(a,b) shows the position of the surface and its second derivative, the bulk and surface currents, the ratio between the surface current and the equilibrium surface current and the different stresses in the Young–Laplace equation, for the two dielectric constants and fixed dimensionless flow rate,  $\Pi_Q = 87.4$ . The Reynolds numbers are not identical, but differences associated with this parameter are small. The equilibrium surface current,  $\tilde{I}_{eq} = 2\pi\varepsilon_0\tilde{R}\tilde{v}_S\tilde{E}_n^o$ , is the limiting value associated with a distribution of charge that fully shields the bulk from the external electric field, i.e. that would make  $\tilde{E}_n^i = 0$  or equivalently  $\tilde{\sigma} = \varepsilon_0\tilde{E}_n^o$ . Using this definition and the surface convection time  $dt = \sqrt{1 + R'^2}(dx/v_S)$ , the equation of conservation of charge (2.5) can be written in the form:

$$\frac{\varepsilon\varepsilon_0/K}{r_c/v_c} \frac{dI_S}{dt} = \frac{\varepsilon}{\pi\Pi_Q^{1/2}} \frac{dI_S}{dt} = I_{eq} - I_S. \quad (3.2)$$

As a fluid particle moves down the surface the surface current approaches the equilibrium value exponentially, with a time constant given by the ratio between the electric relaxation time  $\varepsilon\varepsilon_0/K$  and the flow residence time  $r_c/v_c$ . Fernández de la Mora & Loscertales (1994) used this equation to explain the breakdown of Taylor’s solution when applied to an experimental cone jet: they argued that far upstream from the vertex the electric relaxation time is much smaller than the residence time, the surface current adopts its equilibrium value and the electro-hydrostatic Taylor cone solution is valid. However as the fluid approaches the vertex both times become comparable,  $I_S$  and  $I_{eq}$  differ and a significant electric field develops inside the liquid which, by injecting charge onto the surface, attempts to restore equilibrium. On the

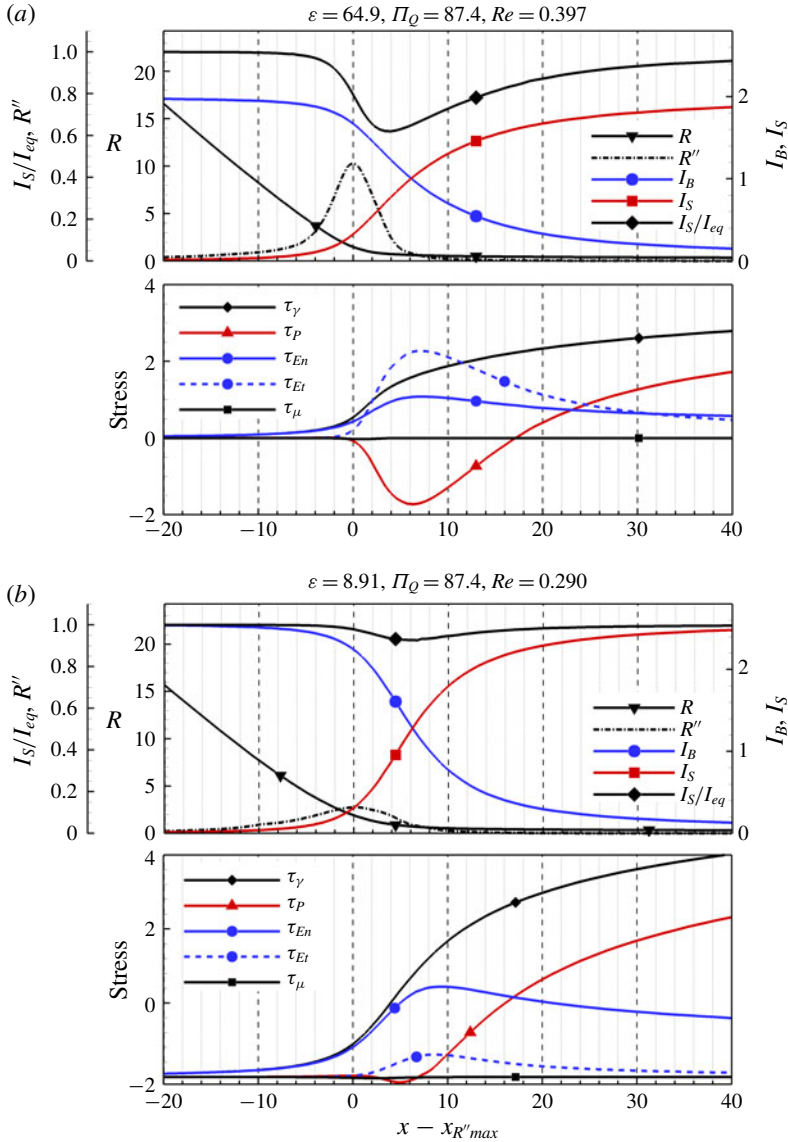


FIGURE 6. (Colour online) Position of the surface and its second derivative, bulk and surface current, ratio between the surface current and its equilibrium value and normal stresses for (a) propylene carbonate,  $\Pi_Q = 87.4$ ,  $Re = 0.40$ , and (b) tributyl phosphate,  $\Pi_Q = 87.4$ ,  $Re = 0.29$ . Equation (2.6) reads  $\tau_\gamma = \tau_P + \tau_\mu + \tau_{En} + \tau_{Et}$  in terms of the labels.

other hand, Gañán-Calvo (1997, 2004) has argued that the position of the free surface is such that  $I_S$  and  $I_{eq}$  are approximately equal everywhere, i.e. that the surface charge is always relaxed or in equilibrium. More recently Gañán-Calvo, Rebollo-Muñoz & Montanero (2013) have proposed that for liquids with  $\varepsilon Re > 1$ , which is the case in this article, the surface charge is not in equilibrium near the minimum flow rate. Figure 6(a,b) shows that the ratio  $I_S/I_{eq}$  departs significantly from one in the region where the cone transitions into a jet, the deficit being larger for the larger dielectric

constant: the minimum value of  $I_S/I_{eq}$  is 0.62 for  $\varepsilon = 64.9$ , and 0.92 for  $\varepsilon = 8.91$ . This is to be expected since at constant  $\Pi_Q$  and almost constant geometry (see figure 5e), the ratio between the electric relaxation and flow residence times is proportional to the dielectric constant. Figures 6(a) and 6(b) also show that, sufficiently upstream of the vertex where the surface charge is in equilibrium ( $I_S/I_{eq} \cong 1$ ), the electrostatic stress component  $\tau_{En}$  fully balances the capillary tension  $\tau_\gamma$  in agreement with Taylor's solution. As  $I_S/I_{eq}$  decreases the stress component  $\tau_{Et}$ , absent in Taylor's equipotential cone, becomes important in the balance of normal stresses, and the surface current increases. the value of  $\tau_{Et}$  is proportional to the dielectric constant, and its high value for propylene carbonate makes  $\tau_{Et}$  larger than  $\tau_{En}$  in the transition region of this liquid; furthermore, to balance this large  $\tau_{Et}$  stress pulling the surface, the pressure becomes significant and negative. Downstream, as the  $I_S/I_{eq}$  ratio returns to one (i.e. the surface charge approaches equilibrium), the surface current asymptotes to the total current, the electric stress asymptotes to a constant or slowly varying value and the balance of stresses is fulfilled by an increasing positive fluid pressure. The normal component of the viscous stress is negligible everywhere. The higher values of  $R''(x)$  for propylene carbonate indicate that the radius of curvature in an interval a few units around  $x_{R''_{max}}$  is smaller than for tributyl phosphate, i.e. at constant dimensionless flow rate the transition from cone to jet in propylene carbonate is sharper than in tributyl phosphate.

Figure 7(a,b) shows  $I_S/I_{eq}$  along the axis at several flow rates, for propylene carbonate ( $Re = 0.397$ ) and tributyl phosphate ( $Re = 1.12$ ) respectively. Figure 7(c) shows the minimum value of  $I_S/I_{eq}$  as a function of  $\varepsilon/(\pi\Pi_Q^{1/2})$ , for all solutions and flow rates simulated. All flow rates in these figures were reproduced in experiments except for the tributyl phosphate solution with  $Re = 1.12$ , which was characterized in the range  $6.23 \leq \Pi_Q \leq 35.1$  (Gamero-Castaño 2010). The lowest flow rate for this solution,  $\Pi_Q = 1$ , is significantly smaller than the minimum at which it was stable. Consistent with the  $\varepsilon/(\pi\Pi_Q^{1/2})$  coefficient in (3.2), the deficit of  $I_S/I_{eq}$  from one accentuates at increasing dielectric constant and decreasing flow rate. The less polar fluid, tributyl phosphate, exhibits the largest minimum values of  $I_S/I_{eq}$ : 0.965 for  $Re = 1.12$ ,  $\Pi_Q = 316.2$ ; and 0.962 for  $Re = 0.290$ ,  $\Pi_Q = 240.7$ . At these conditions, the surface charge is very near its equilibrium value everywhere along the cone-jet's surface. On the other hand propylene carbonate, with its large dielectric constant, exhibits the states observed in experiments with smallest values of  $I_S/I_{eq}$ : 0.421 for  $Re = 0.74$ ,  $\Pi_Q = 20.0$ ; and 0.560 for  $Re = 0.397$ ,  $\Pi_Q = 59.3$ . The surface charge along the transition region under these conditions is far from equilibrium. Between these two extreme cases, the shortfall of the surface charge from equilibrium is primarily governed by the value of  $\varepsilon/(\pi\Pi_Q^{1/2})$ .

Figure 8 shows the radius of the cone jet at two significant axial positions: at the current cross-over,  $R_X$ ; and at the point where the ratio  $I_S/I_{eq}$  falls by 10% of its maximum drop,  $R_B$ . The latter is a reference point for the breakdown of Taylor's solution.  $R_X$  depends very slightly on the dielectric constant, while  $R_B$  increases moderately with  $\varepsilon$ . Both radii are insensitive to the Reynolds number. They are also insensitive to variations of the flow rate in the range in which the cone jet is stable, while both radii increase at decreasing  $\Pi_Q$  for the two lowest flow rates of the  $\varepsilon = 8.91$ ,  $Re = 1.12$  case. These two lower flow rates are below the minimum observed in experiments. Thus, the scale  $r_c$  is not only the correct characteristic radial length throughout the transition region, but when the radius of the surface is expressed in  $r_c$  units, its value at significant axial points depends very slightly on the dimensionless numbers parametrizing the solution. Note that, although  $R_B$  is defined

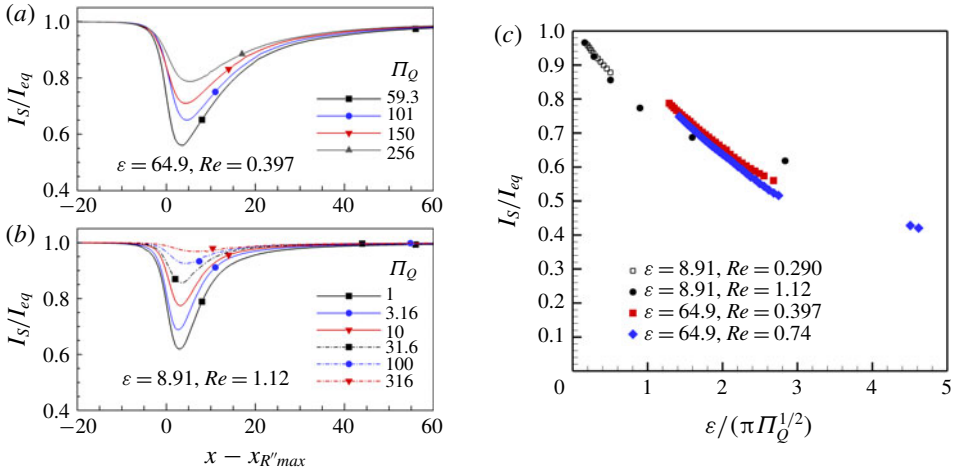


FIGURE 7. (Colour online) Ratio between the surface current and its equilibrium value as a function of axial position and at several flow rates for (a) propylene carbonate and  $Re=0.397$ , and (b) tributyl phosphate and  $Re=1.12$ . (c) Minimum value of the  $I_S/I_{eq}$  ratio versus  $\varepsilon/(\pi\Pi_Q^{1/2})$ , for tributyl phosphate ( $\varepsilon=8.91$ ) and propylene carbonate ( $\varepsilon=64.9$ ).

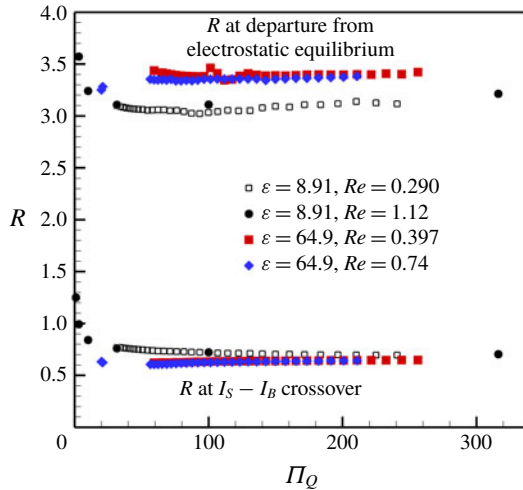


FIGURE 8. (Colour online) Radius of the cone jet at the current cross-over, and typical value in the area where surface charge equilibrium breaks down, as a function of the dimensionless flow rate.

at the onset of charge relaxation effects, the radius of the surface in this region scales with  $r_c$  instead of  $r_{FM}$ . This suggests that the coupling between the different variables throughout the transition region may reduce the validity of the local balance used by Fernández de la Mora & Loscertales (1994) to derive the characteristic length  $r_{FM}$ .

Figure 9 shows the axial extent  $L$  of the transition region as a function of the dimensionless flow rate.  $L$  is defined as the length of the interval where the surface current changes from 5% to 95% of its final value. While the dependency on the

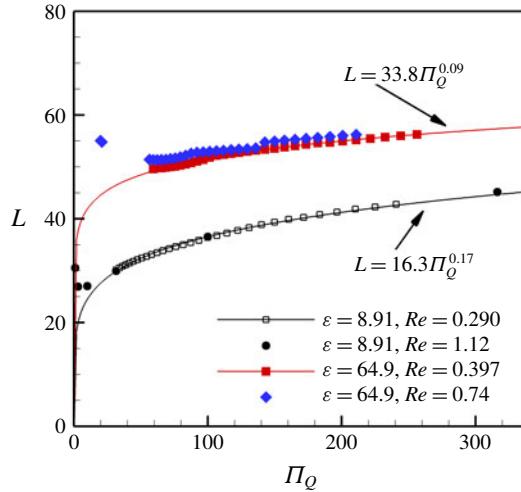


FIGURE 9. (Colour online) Length of the transition region as a function of the dimensionless flow rate.

Reynolds number is insignificant, the dielectric constant has a strong effect on the value of  $L$ . At constant  $\Pi_Q$  and increasing  $\varepsilon$ , the larger ratio between the electric relaxation and the flow residence times slows down the merging of the surface current with its equilibrium value, and a longer transition region is needed to equilibrate the surface charge.  $L$  is a relatively weak function of  $\Pi_Q$ : a power fit yields  $L \sim \Pi_Q^{0.09}$  for propylene carbonate, and  $L \sim \Pi_Q^{0.17}$  for tributyl phosphate. This indicates that  $r_c$  is a good scale for the axial extent  $L$  of the transition region and, being also the characteristic length in the radial direction, the shape of the transition region scaled with  $r_c$ , is relatively invariant to changes of  $\Pi_Q$  and  $Re$ . Since these dimensionless numbers are present in the model equations and parametrize the solutions, the near invariant shape of the transition region is a surprising fact. The large values that  $\Pi_Q$  adopts in typical electrospraying conditions may contribute to this unexpected property.

Figure 10(a,b) shows the maximum values of the normal and tangential components of the outer electric field at the surface of the cone jet. The maxima are located slightly downstream of the current cross-over. The electric field decreases slightly at increasing dielectric constant, and is a very weak function of the Reynolds number. A power fit of the tangential component yields  $E_{t,max} \sim \Pi_Q^{0.06}$  for propylene carbonate, and  $E_{t,max} \sim \Pi_Q^{0.09}$  for tributyl phosphate. This weak dependence is to be expected from the definition of the  $E_c$  scale, which is based on the characteristic tangential component in the transition region:

$$\tilde{E}_{t,max} \cong \frac{\tilde{I}}{2\pi\tilde{R}_X^2K} = \frac{I}{2R_X^2} \frac{I_c}{\pi r_c^2 K} = \frac{I}{2R_X^2} E_C \tag{3.3}$$

since both  $I$  and  $R_X$  are weak functions of the dimensionless flow rate,  $E_{t,max}$  must also be a weak function of  $\Pi_Q$ . The normal component scales as  $E_{n,max}^o \sim \Pi_Q^{0.48}$  for propylene carbonate and  $E_{n,max}^o \sim \Pi_Q^{0.44}$  for tributyl phosphate, i.e. nearly as the square root of the dimensionless flow rate. This dependence is also to be expected because

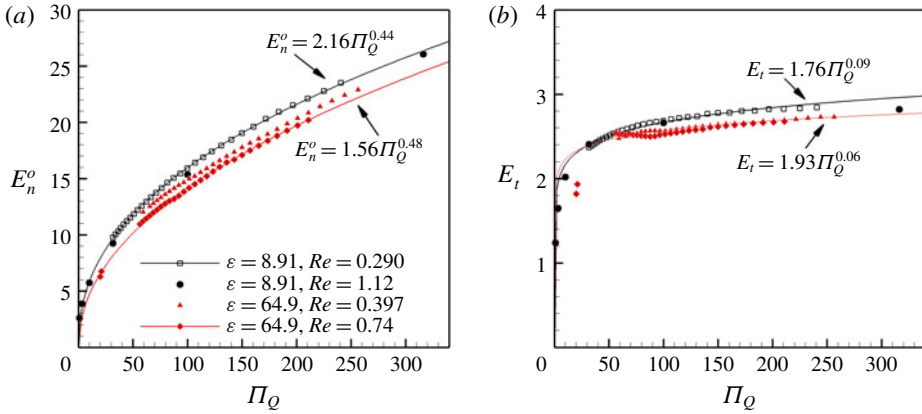


FIGURE 10. (Colour online) Maximum values of the normal (a) and tangential (b) components of the electric field at the surface of the cone jet, on the vacuum side.

at the current cross-over the surface current equals the bulk conduction current, and the surface charge is of the order of  $\epsilon_0 E_n^o$ :

$$\tilde{E}_{n,max}^o \cong \frac{\tilde{\sigma}}{\epsilon_0} \cong \frac{2\tilde{I}}{2\pi\tilde{R}_x\tilde{v}_s\epsilon_0} = \frac{\tilde{I}\tilde{R}_x}{\epsilon_0 Q} = \pi I R_x E_C \Pi_Q^{1/2}. \tag{3.4}$$

Gañán-Calvo (2004) originally put forward the same arguments to establish the scaling of  $\tilde{E}_{t,max}$  and  $\tilde{E}_{n,max}^o$ . On the other hand, he argues for a scaling for the axial length,  $\tilde{L}_{G-C} \sim \gamma / (\epsilon_0 \tilde{E}_t^2) \sim (\epsilon_0^2 \gamma / \rho K^2)^{1/3} \Pi_Q$ , which is different from the scaling observed in figure 9,  $\tilde{L} = f(\epsilon) (\epsilon_0^2 \gamma / \rho K^2)^{1/3} \Pi_Q^{(1/2)+\beta}$ , with  $\beta$  equal to 0.09 and 0.17 for propylene carbonate and tributyl phosphate respectively, i.e. values significantly smaller than the 1/2 required to match Gañán-Calvo’s scaling.

The voltage source connected to the emitter injects electric power in the cone jet, which is converted into jet kinetic energy, ohmic and viscous dissipation, surface energy, etc. This balance is important to understanding the physics of electrospaying, e.g. Gañán-Calvo & Montanero (2009) use a simplified energy balance to derive the  $r_c$  scale (the authors assume that the electric power injected within the transition region is mostly transformed into jet kinetic power). The following balance can be derived by integrating the equation of mechanical energy over a volume  $\Pi_x$  like the one in figure 1 bounded by surfaces  $\Sigma_2^i$ ,  $\Sigma_1$ , and a surface  $\Sigma_x$  that intersects  $\Sigma_1$  downstream at  $\{x, r = R(x)\}$ :

$$\begin{aligned} \tilde{I}\tilde{\phi}_S(x_o) - \left( \tilde{I}_S\tilde{\phi}_S(x) + \int_{\Sigma_x} \tilde{\phi}_i d\tilde{I}_C \right) &= \tilde{P}_\Omega + \tilde{P}_\mu + \left( \int_{\Sigma_x} \frac{\rho\tilde{v}^2}{2} \tilde{\mathbf{v}} \cdot d\tilde{\mathbf{A}} - \int_{\Sigma_2^i} \frac{\rho\tilde{v}^2}{2} \tilde{\mathbf{v}} \cdot d\tilde{\mathbf{A}} \right) \\ + \left( \int_{\Sigma_x} \tilde{p}\tilde{\mathbf{v}} \cdot d\tilde{\mathbf{A}} - \int_{\Sigma_2^i} \tilde{p}\tilde{\mathbf{v}} \cdot d\tilde{\mathbf{A}} \right) &+ \left( \int_{\Sigma_2^i} (\tilde{\boldsymbol{\tau}} \cdot \tilde{\mathbf{v}}) \cdot d\tilde{\mathbf{A}} - \int_{\Sigma_x} (\tilde{\boldsymbol{\tau}} \cdot \tilde{\mathbf{v}}) \cdot d\tilde{\mathbf{A}} \right). \end{aligned} \tag{3.5}$$

The left-hand side is the electric power supplied to  $\Pi_x$ . When  $\Sigma_x$  is an equipotential surface (e.g. a plane perpendicular to the axis placed sufficiently downstream), this term adopts the more obvious form  $\tilde{I}[\tilde{\phi}_S(x_o) - \tilde{\phi}_S(x)]$ . The first and second terms



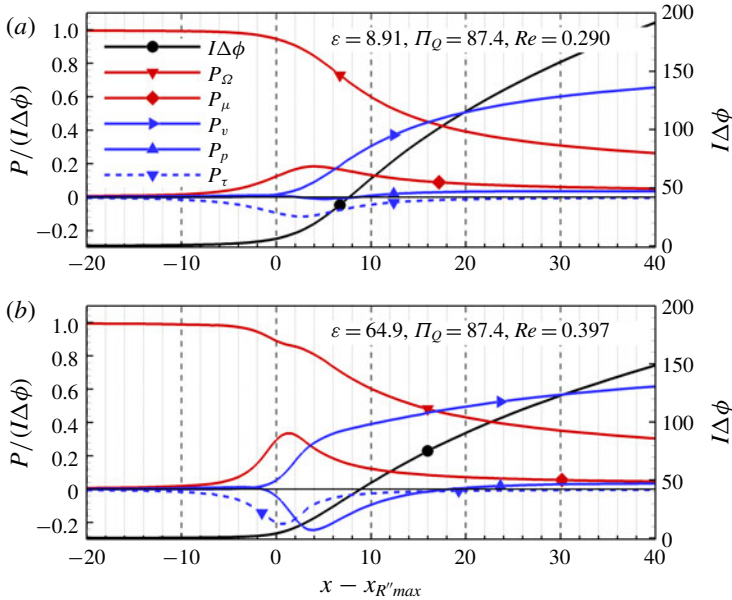


FIGURE 11. (Colour online) Macroscopic energy balance in the cone jet up to a given axial position. In terms of the labels, equation (3.5) reads  $I\Delta\phi = P_\Omega + P_\mu + P_v + P_p + P_\tau$ . Panels (a) and (b) are for tributyl phosphate at  $Re = 0.29$  and propylene carbonate at  $Re = 0.397$ , at fixed flow rate  $\Pi_Q = 87.4$ .

on the right-hand side are the ohmic,  $\tilde{P}_\Omega = \int_{\Pi_x} (\tilde{\mathbf{E}} \cdot \mathbf{K}\tilde{\mathbf{E}}) d\tilde{V}$ , and viscous dissipation,  $\tilde{P}_\mu = \int_{\Pi_x} (\tilde{\boldsymbol{\tau}} : \nabla\tilde{\mathbf{v}}) d\tilde{V}$ . The kinetic energy density, pressure and viscous stress are negligible far upstream at  $\Gamma_2^i$ , and can be omitted. Figure 11 shows the electric power in  $I_C\phi_c$  units as a function of the axial coordinate, and the terms on the right-hand side divided by the electric power. The electro spraying parameters are the same as in figures 6 and 5(e). The integrals in (3.5) are computed on  $\Sigma_x$  surfaces defined by lines of constant  $\xi$ , see figure 3. Early in the transition region, e.g. at  $x - x_{R'_{max}} = 0$ , the electric power is mostly converted into ohmic dissipation, 94% for  $\varepsilon = 8.91$  and 89% for  $\varepsilon = 64.9$  (we will continue listing values for the two dielectric constant cases in this order), and viscous dissipation, 12% and 29%; the conversion into jet kinetic energy is small, 1% and 5%. The sum of the three terms exceed 100% because the viscous stress flow power at this point is a relatively large and negative, -9% and -19% (the viscous stress is doing work on the fluid), while the values of the pressure flow power are 1% and -4%. Dissipation still accounts for most of the electric power at the current cross-over ( $x - x_{R'_{max}} = 6.2$  and 6.1), with combined values of 92% and 91%; at this point the values of jet kinetic power are 17% and 33%. As the fluid moves further downstream and the current increasingly becomes surface current, the conversion of electric energy into kinetic energy is more efficient. For example, at the point where the surface current reaches 95% of its final value,  $x - x_{R'_{max}} = 31.8$  and 68.1, the conversion into kinetic energy is 61% and 70%, while the combined dissipation is 36% and 27% (the balance is completed by a small positive value of the pressure flow power). The profiles of the jet kinetic power are different for the two liquids, having an earlier and steeper increase for propylene carbonate associated with the simultaneous negative pressure flow power: as

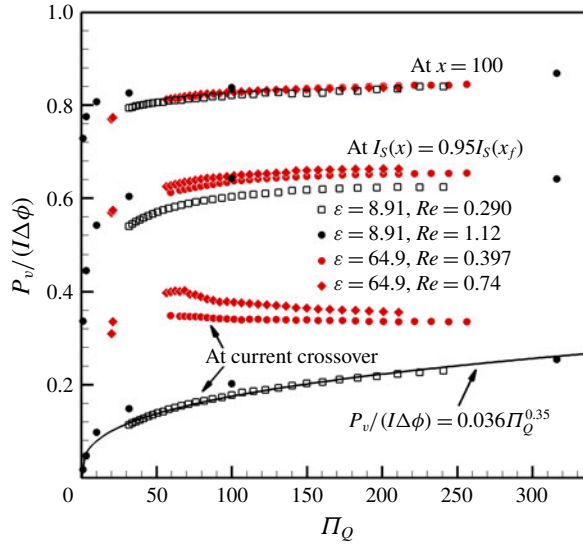


FIGURE 12. (Colour online) Ratio between jet kinetic and electric powers, computed in a macroscopic energy balance extended up to the current cross-over axial location, the point where the surface current reaches 95 % of its final value, and 100 units downstream from  $x_{R''_{max}}$ .

seen in figure 6, propylene carbonate exhibits a large negative pressure peak around the current cross-over, induced by the large  $(\varepsilon - 1)\varepsilon_0\tilde{E}_t^2$  normal pulling stress. This pressure profile accelerates the fluid up to the pressure minimum, and slows it down thereafter. The earlier rise of the jet kinetic power requires, from mass conservation, a smaller cone-jet radius in the initial section of the transition region. This is indeed observed in figure 5(e), where the surface of propylene carbonate falls below that of tributyl phosphate, and exhibits a sharper transition from cone to jet; the sharper transition, or smaller radii of curvature, is more evidently inferred from the higher values of  $R''(x)$  in figure 6(a). A similar sharper transition occurs in figure 5(c,d) at decreasing flow rate for fixed dielectric constant. The correlation of the sharpness of the transition with flow rate and dielectric constant is due to the varying intensity of charge relaxation, as given by the ratio  $\varepsilon/\Pi_Q^{1/2}$  in (3.2). When  $\varepsilon/\Pi_Q^{1/2}$  is large, the surface current can be significantly smaller than its equilibrium value, and the surface will remain closer to the ideal conical shape farther towards the axis; on the other hand when  $\varepsilon/\Pi_Q^{1/2}$  is small, the surface charge approaches equilibrium earlier in the transition region, which is only possible if the surface separates upward from the electrostatic conical shape.

Figure 12 shows the ratio between jet kinetic and electric powers as a function of the dimensionless flow rate, at three axial locations: the current cross-over, the point where the surface current is 95 % of its final value and 100 units downstream from  $x_{R''_{max}}$ . At the current cross-over, i.e. at approximately the midsection of the transition region, as little as 9 % of the electric power is converted into jet kinetic power for tributyl phosphate near the minimum flow rate, and 26 % at the largest flow rate investigated; the fraction is larger for propylene carbonate, approximately 35 %, due to the acceleration of the flow by the negative pressure peak. Towards the end of the transition region the transitory effect of the negative pressure profile of propylene

carbonate has disappeared and the conversion, with values between 54 % and 65 % depending on the flow rate, is similar for both liquids. The balance is dissipated. The power dissipated increases very slightly further downstream (the bulk current is small while viscous dissipation is only significant early in the transition region around the maximum of  $R''(x)$ ), most of the electric power injected in this downstream region is converted into kinetic energy, and the ratio increases monotonically. The conversion into kinetic energy never reaches 100 % due to the fraction of the electrical power that is dissipated mostly within the transition region. As mentioned above, in order to derive the  $r_c$  scale Gañán-Calvo & Montanero (2009) assume that the electric power injected within the transition region is mostly transformed into jet kinetic power. Although it is not clear at which point of the transition region this balance should be approximately fulfilled, we think that the current cross-over point is the correct location because the derivation also assumes a total current that is of the order of the conduction current. Although the conversion into kinetic energy at the cross-over is relatively small, especially for tributyl phosphate, we think that the argument by Gañán-Calvo and Montanero remains valid because the jet's kinetic power is in any case of the order of the electric power.

#### 4. Conclusions

We have solved numerically the leaky-dielectric model applied to cone jets, for operational parameters typical of experimental conditions. The main novelty compared to previous work is the application of the least-squared weighted residual method to the Young–Laplace equation, in order to find the position of the free surface. The numerical solution is validated with measurements of the electric current. The model yields a universal solution that only depends on the physical properties and the flow rate of the liquid. This is made possible by employing Taylor's electric potential as a far-field boundary condition. The solution in dimensionless form is a function of three dimensionless numbers: the dimensionless flow rate  $\Pi_Q$ , the electrohydrodynamic Reynolds number  $Re$  and the dielectric constant  $\varepsilon$ .

The current emitted by the electrospray follows the linear law  $\tilde{I} = a(\rho K Q / \varepsilon \varepsilon_0)^{1/2} + b$ , where  $a$  and  $b$  are functions of the dielectric constant. For the two liquids studied, tributyl phosphate ( $\varepsilon = 8.91$ ) and propylene carbonate ( $\varepsilon = 64.9$ ),  $b$  is negative and decreases with increasing dielectric constant. The position of the surface in the transition region scales well with the characteristic length  $r_c$ , both in the radial and axial direction. Thus the surface, when plotted in  $r_c$  units, remains largely unchanged regardless of the values of  $\Pi_Q$ ,  $Re$  and  $\varepsilon$ . The diameter of the jet at the current cross-over point is always near  $0.67r_c$ , for all simulated values of  $\Pi_Q$ ,  $Re$  and  $\varepsilon$ . The maximum value of the normal component of the electric field on the outer side of the surface scales with  $(\gamma^{5/2}/(\varepsilon_0\rho K^{1/2}Q^{3/2}))^{1/3}\Pi_Q^{1/2}$ , while the maximum value of the tangential component scales with  $(\gamma^{5/2}/(\varepsilon_0\rho K^{1/2}Q^{3/2}))^{1/3}$ . Both take place slightly downstream of the cross-over between the surface and bulk currents. A large fraction of the electric energy transferred within the transition region is dissipated, and conversion into kinetic energy only exceeds dissipation as most of the electric current becomes fixed on the surface (i.e. within the transition region but well downstream of the current cross-over, e.g.  $x - x_{R''_{max}} = 19.42$  and  $20.45$  in figure 11).

The surface charge drops below its equilibrium value in the transition region. This is directly demonstrated by the  $I_S/I_{eq}$  profiles in figure 7. The deficit of the surface current with respect to its equilibrium value increases with the ratio  $\varepsilon/(\pi\Pi_Q^{1/2})$ , i.e. with the ratio between the electric relaxation and the flow residence times. Three

characteristics of the cone jet are unequivocal functions of the dielectric constant: (i) the axial length needed to equilibrate the surface current increases with the dielectric constant (on the other hand, the dielectric constant plays a very minor role, if any at all, in the scaling of the radial length); (ii) the asymptotic value of the current at large flow rate (i.e. the slope in the linear law for  $\tilde{I}$ ) decreases at increasing dielectric constant; and (iii) the radius of curvature of the surface in the transition from cone to jet decreases at increasing dielectric constant. Since the dielectric constant appears in the model equations as a factor multiplying the electric field inside the liquid, specifically its component normal to the surface, any dependency on  $\varepsilon$  is indicative of the importance of the term  $\varepsilon E_n^i$  in (2.8b), and therefore of the importance of charge relaxation effects.

### Acknowledgements

This research was supported by NASA's Space Technology Research Early Stage Innovations program, grant NNX17AD01G, and by NSF's Fluid Dynamics program, grant CBET-1604163.

### REFERENCES

- BAKR, A. A. 1986 *The Boundary Integral Equation Method in Axisymmetric Stress Analysis Problems*, Lecture Notes in Engineering, chap. II. Springer.
- BORRAJO-PELAEZ, R., SAIZ, F. & GAMERO CASTAÑO, M. 2015 The effect of the molecular mass on the sputtering of Si, SiC, Ge, and GaAs by electrospayed nanodroplets at impact velocities up to  $17 \text{ km s}^{-1}$ . *Aerosol Sci. Technol.* **49**, 256–266.
- CLOUPEAU, M. & PRUNET-FOCH, B. 1989 Electrostatic spraying of liquids in cone-jet mode. *J. Electrostat.* **22**, 135–159.
- CLOUPEAU, M. & PRUNET-FOCH, B. 1990 Electrostatic spraying of liquids. Main functioning modes. *J. Electrostat.* **25**, 165–184.
- FENN, J. B., MANN, M., MENG, C. K., WONG, S. K. & WHITEHOUSE, C. M. 1989 Electropray ionization for mass spectrometry of large biomolecules. *Science* **246**, 64–71.
- FERNÁNDEZ DE LA MORA, J. 2007 The fluid dynamics of Taylor cones. *Annu. Rev. Fluid Mech.* **39**, 217–243.
- FERNÁNDEZ DE LA MORA, J. & LOSCERTALES, I. G. 1994 The current transmitted through an electrified conical meniscus. *J. Fluid Mech.* **260**, 155–184.
- FLETCHER, C. A. J. 1988 *Computational Techniques for Fluid Dynamics*, Springer Series in Computational Physics, chap. XII–XIII. Springer.
- GAMERO-CASTAÑO, M. 2010 Energy dissipation in electrosprays and the geometric scaling of the transition region of cone-jets. *J. Fluid Mech.* **662**, 493–513.
- GAMERO-CASTAÑO, M. & HRUBY, V. 2002 Electric measurements of charged sprays emitted by cone-jets. *J. Fluid Mech.* **459**, 245–276.
- GAÑÁN-CALVO, A. M. 1997 Cone-jet analytical extension of Taylor's electrostatic solution and the asymptotic universal scaling laws in electro spraying. *Phys. Rev. Lett.* **79**, 217–220.
- GAÑÁN-CALVO, A. M. 2004 On the general scaling theory for electro spraying. *J. Fluid Mech.* **507**, 203–212.
- GAÑÁN-CALVO, A. M., DÁVILA, J. & BARRERO, A. 1997 Current and droplet size in the electro spraying of liquids. Scaling laws. *J. Aerosol. Sci.* **28**, 249–275.
- GAÑÁN-CALVO, A. M., LÓPEZ-HERRERA, J. M., HERRADA, M. A., RAMOS, A. & MONTANERO, J. M. 2018 Review on the physics of electro spray: from electrokinetics to the operating conditions of single and coaxial Taylor cone-jets, and AC electro spray. *J. Aerosol. Sci.* **125**, 32–56.
- GAÑÁN-CALVO, A. M. & MONTANERO, J. M. 2009 Revision of capillary cone-jet physics: electro spray and flow focusing. *Phys. Rev. E* **79**, 066305.

- GAÑÁN-CALVO, A. M., REBOLLO-MUÑOZ, N. & MONTANERO, J. M. 2013 The minimum or natural rate of flow and droplet size ejected by Taylor cone-jets: physical symmetries and scaling laws. *New J. Phys.* **15**, 033035.
- GRUSTAN-GUTIERREZ, E. & GAMERO-CASTAÑO, M. 2017 Microfabricated electrospray thruster array with high hydraulic resistance channels. *J. Propul. Power* **33**, 984–991.
- HERRADA, M. A., LÓPEZ-HERRERA, J. M., GAÑÁN-CALVO, A. M., VEGA, E. J., MONTANERO, J. M. & POPINET, S. 2012 Numerical simulation of electrospray in the cone-jet mode. *Phys. Rev. E* **86**, 026305.
- HIGUERA, F. J. 2003 Flow rate and electric current emitted by a Taylor cone. *J. Fluid Mech.* **484**, 303–327.
- LOSCERTALES, I. G., BARRERO, A., GUERRERO, I., CORTIJO, R., MARQUEZ, M. & GAÑÁN-CALVO, A. M. 2002 Micro/nano encapsulation via electrified coaxial liquid jets. *Science* **295**, 1695–1698.
- MELCHER, J. R. & TAYLOR, G. I. 1969 Electrohydrodynamics: a review of the role of interfacial shear stresses. *Annu. Rev. Fluid Mech.* **1**, 111–146.
- SAVILLE, D. A. 1997 Electrohydrodynamics: the Taylor–Melcher leaky dielectric model. *Annu. Rev. Fluid Mech.* **29**, 27–64.
- SUN, D., CHANG, C., LI, S. & LIN, L. 2006 Near-field electrospinning. *Nano Lett.* **6**, 839–842.
- TAYLOR, G. I. 1964 Disintegration of water drops in an electric field. *Proc. R. Soc. Lond. A* **280**, 383–397.